

High Quality Inkjet Printed-Emissive Nanocrystalline Perovskite CsPbBr₃ Layers for Color Conversion Layer and LEDs Applications

Giovanni Vescio,* Juan Luis Frieiro, Andrés F. Gualdrón-Reyes, Sergi Hernández, Iván Mora-Seró, Blas Garrido, and Albert Cirera

Metal halide perovskites (MHPs) have shown outstanding optical emissive properties and can be employed in several optoelectronics devices. In contrast with materials of well-established technologies, which are prone to degradation or require expensive processes, MHPs can be obtained by solution processing methods and increase stability. Inkjet printing is proposed as an industrial friendly technique to deposit MHPs. The inks have been developed from colloidal CsPbBr₃ nanocrystals and printing procedures that allow the deposition of thin layers with intense green emission. High emissive printed layers are assured by carrying out thermal annealing in vacuum oven, which is demonstrated to promote compact layers with low roughness, corroborated by SEM and AFM. XRD measurements show CsPbBr₃ crystalline layers with cubic symmetry and XPS provides insight into the stoichiometric composition and local bonding. Optical properties of inkjet-printed CsPbBr₃ films have been analyzed by UV–vis absorbance and photoluminescence (PL), to extract the bandgap energy and photoluminescence quantum yield (PLQY). CsPbBr₃ printed layers emit at 524 nm with a narrow emission (FWHM ≈ 15 nm), exhibiting a PLQY up to 20%. These results enabled the large-scale fabrication by inkjet printing of CsPbBr₃ color conversion layers (CCLs) and pave the way for flexible LEDs.

1. Introduction

Emerging solution processed metal halide perovskite (MHP) materials, either inorganic or hybrid organic-inorganic, have been

shown competitive and even superior to organic materials and related technologies for optoelectronic and photovoltaic applications.^[1–3] Among other drawbacks, organic light-emitting diodes (OLEDs) can degrade fast, especially blue-emitting OLEDs, and are fabricated with complex and expensive technologies which require advanced lithography and clean room environment.^[4–7]

In contrast, cost-effective solution processable methods not requiring lithography and based on MHPs have been recently used to produce large-area, highly efficient and low-cost optoelectronic devices and solar cells.^[8] MHPs are especially well-suited for solution processable methods because of their easy synthesis at low temperature, defect tolerance, high absorption capability, tunability of bandgap energy within the visible and near infrared ranges, high photoluminescence quantum yield (PLQY), narrow emission peak, good transport properties and a low density of non-radiative recombination centers.^[9–13] As an example, efficient perovskite light emitting diodes (PeLEDs) have been reported in the literature.^[2,14–17]


with emissions in the visible range. The first PeLED reported in 2014 had an external quantum efficiency (EQE) of about 0.1% (hybrid methylammonium lead bromide, MAPbBr₃)^[18] and the evolution has been extremely fast with EQEs higher than 21% reported so far, comparable to that of state-of-the art OLEDs.^[2,19]

The huge progress on PeLEDs is based on several improvements at material and device engineering levels. At material level, this has mainly been due to the use of quantum-confined nanocrystals (NCs) which provide higher recombination yield to injected electron and holes, allowing also the possibility for bandgap engineering by controlling just their size.^[20] The preparation of MHP (NCs) with unity PLQY along the whole visible spectra has boosted the interest of these materials for light emitting applications.^[13] Moreover, since the pioneering works of Kovalenko and co-workers on all inorganic nanocrystals of CsPbX₃ (X = Cl, Br, I)^[20] colloidal solutions based on nanocrystals have become an outstanding choice to produce layers based on those materials. For visible LEDs, the most used and obvious choice is CsPbBr₃, which exhibit a bandgap in the green part of the visible spectrum and emission at a wavelength around 515 nm with FWHM as narrow as 20 nm.^[21–24]

G. Vescio, J. L. Frieiro, S. Hernández, B. Garrido, A. Cirera
MIND-IN2UB
Department of Electronics and Biomedical Engineering
Universitat de Barcelona
Martí i Franquès 1, Barcelona 08028, Spain
E-mail: gvescio@ub.edu

A. F. Gualdrón-Reyes, I. Mora-Seró
Institute of Advanced Materials (INAM)
Universitat Jaume I (UJI)
Avenida de Vicent Sos Baynat, s/n, Castelló de la Plana 12071, Spain

A. F. Gualdrón-Reyes
Universidad Austral de Chile
Facultad de Ciencias
Instituto de Ciencias Químicas
Isla Teja, Valdivia 5090000, Chile

 The ORCID identification number(s) for the author(s) of this article can be found under <https://doi.org/10.1002/admt.202101525>.

DOI: 10.1002/admt.202101525

However, most of these materials (and their corresponding devices) have been obtained with solution deposition techniques, mainly spin coating, difficult to upscale. In contrast, inkjet printing is an industrial friendly technique which provides a method to produce low-cost, large-area, lightweight and foldable devices.^[25–28] Since its early beginnings, inkjet printing has attracted the attention of many researchers in the perovskite materials field.^[8,29–33] The difficulties of inkjet printing technique are mainly related with ink engineering, substrate compatibility and multistack layering^[29] and have limited so far the development of MHPs devices. The main challenges with these materials remain in printing large-area defect-free layers without pinholes and the complexity of achieving high quality interfaces with transport layers. Among the techniques used to improve the quality of the printed layers, a vacuum-assisted oven process after the inkjet printing has been shown to give as good results as the anti-solvent process during spin coating.^[29,30] It has been stated that partial crystallization of the liquid film before vacuum annealing will result in substantial degradation of the film quality.^[31,34] Maintaining a liquid film before annealing and thus prolonging the crystallization time during the vacuum annealing could be one of the key factors to produce inkjet-printed perovskite-based devices.^[35] Nevertheless, recent progress has been made in the field like that of Hermerschmidt et al. who claimed the first inkjet-printed metal halide organic MAPbBr₃ perovskite devices^[31] emitting up to 8000 cd m⁻². Furthermore, D. Li et al. reported the deposition of inkjet-printed FA(Cs)PbBr₃ layers with promising devices with EQE up to 2.8%,^[33] whereas Shi et al. demonstrated perovskite nanocomposite arrays.^[32]

Very few articles on inkjet-printed CsPbBr₃ layers based on nanocrystals can be found in the literature.^[36–39] M. Duan et al. reported inkjet-printed CsPbBr₃ NCs embedded into monomers and photoinitiators, showing promising performance for color conversion layers (CCLs), albeit very thick layers into a pre-patterned areas and UV curing are required.^[38] Similarly, C. Zheng et al. demonstrated PeLEDs using single nozzle printing on a pixel pit structure.^[40] Other approaches are based on printing or depositing over scaffolds of mesoporous silica^[39] and/or core-shell structures or encapsulation with polymers to protect the NCs.^[36,41,42] Despite the many benefits of CsPbBr₃ in terms of emissivity (high PLQY and narrow emission peak) and stability (fully inorganic but low stability in polar media),^[43] there is still an uncertainty of its deposition for large scale area via inkjet printing and its properties after been annealed with a complete structural characterization. This work paves the way to its use and intends to give clear solutions to common problems in inkjet engineering such as the optimal best required post-process annealing treatment by an in depth morphological, chemical, and optical characterization to ensure large scale production on flexible substrate without any pre-patterned structure.

In this work, we show the approach for the formulation of suitable inks for inkjet printing based on colloidal CsPbBr₃ NCs focusing on the importance of the following post-process annealing. After exploring different ink formulations, we found the mixing of high and low boiling point solvents (dodecane and hexane, respectively) as an appropriated system.^[8,35] This fact shows the best combination of ink stability and optimal printability, that is, an improved performance of the printed layer due to the good wettability of the CsPbBr₃ NCs ink. Furthermore,

we have studied different printing strategies and procedures by adjusting patterns, velocity, temperature, and post-processing of the layers to optimize their morphological quality, while maximizing their light emission. Once the inks and the printing procedure have been optimized, we pay attention to the relevance of the post-deposition temperature treatment to achieve the best uniformity and optical properties. The annealing in vacuum in an oven is proved to produce high quality layers in contrast with results obtained on a hotplate or in a convection furnace in air of this and previous relevant works. By using a systematic characterization employing a broad range of techniques (AFM, SEM, XRD, FTIR, XPS, PL, absorption), we have been able to measure and define the properties of the printed layers. Indeed, this characterization has given feedback to optimize formulation and printing until achieving uniform, pinhole-free, compact layers with high emission yield. The analysis reveals that optimum inkjet-printed CsPbBr₃ NC layers are homogeneous at large scale without any detrimental defects like pinholes or propagation of printing errors such as large wrinkles or fractures among grains. As a proof-of-concept, we demonstrate how these layers can directly act as CCL to develop green all-inorganic fully inkjet-printed LEDs.^[44,45]

2. Results and Discussion on Inkjet Printed CsPbBr₃ Layers

2.1. Stability and Printability of CsPbBr₃ Ink

The perovskite CsPbBr₃ NCs ink is obtained by mixing a high-boiling point solvent, dodecane, and a low-boiling point solvent, hexane (3:1 ratio, respectively) at a concentration of 20–30 mg mL⁻¹ which ensures a stable jettability of the droplet. Dynamic light scattering (DLS) was used for the estimation of NC size distribution of the proposed ink. The results of the average calculation of the NCs size indicate that CsPbBr₃ NCs are mono-dispersed with uniform particle size, values around 7 nm, which indicates that the material is well dispersed (Figure S1, Supporting Information). In general, for inkjet-printing, the size of the dispersed nanomaterials in the ink should be smaller than 1/50 of the nozzle diameter, δ ,^[46] to prevent the clogging of the nozzle.^[47] The drop formation is influenced by the rheology parameters, such as density (ρ), viscosity (η), and surface tension (γ), which consider the inertial, viscous and surface tension forces, respectively. These parameters are required to estimate the quality of the ejected drop, expressed by the correlated dimensionless figure of merit (FOM) Z number^[48] given by Equation (1). This FOM is equivalent to the inverse of the Ohnesorge (Oh) parameter^[48] and independent of fluid velocity:^[48]

$$Z = \frac{1}{Oh} = \frac{\sqrt{\delta \cdot \rho \cdot \gamma}}{\eta} \quad (1)$$

The analysis of surface tension, viscosity, and density of the ink carried out results in 27 dynes cm⁻¹, 2.5 cPs and 1.08 g cm⁻³, respectively. For our CsPbBr₃ ink, considering the rheology parameters (Table S2, Supporting Information), the estimated value of Z is Z = 12, which falls within the assumed optimal range, 1 < Z < 14,^[49] predicting the formation of a stable droplets (Video S1 and Figure S2, Supporting Information).

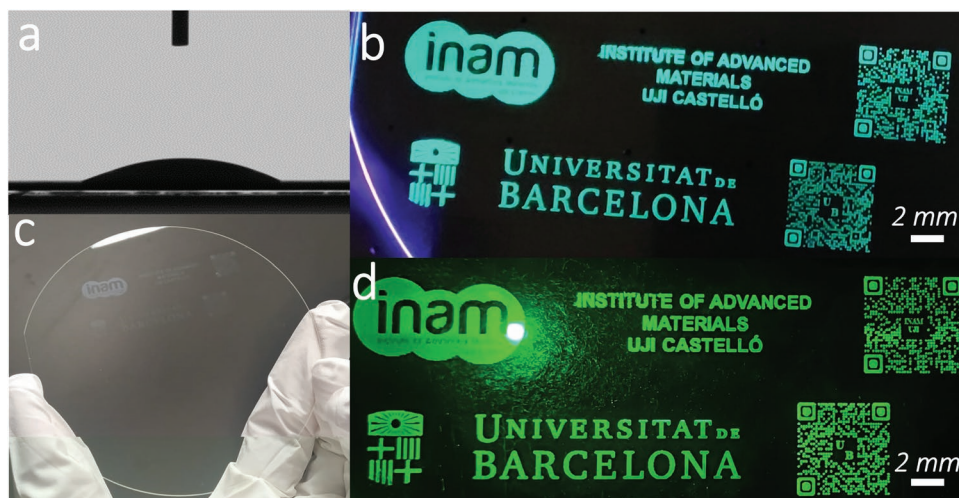


Figure 1. a) Good wettability CsPbBr₃ NCs ink on fused silica by a contact angle value of $\approx 25^\circ$; b) optical image of the as inkjet-printed CsPbBr₃ NCs ink (wet film) of a pattern on transparent PI flexible substrate; c) pattern under ambient light which is transparent: CsPbBr₃ NCs inkjet-printed layer on fused silica; d) detail of the fluorescent emission of printed CsPbBr₃ NCs after annealing.

All the above-mentioned parameters are crucial in order to ensure uniform, low-roughness CsPbBr₃ NCs thin films avoiding the coffee ring effect due to the preferential evaporation at the contact line which promotes an outward flow driving the NCs to the edge.^[50,51] To solve this undesired effect, the solution and opposite phenomena is the promotion of an inward Marangoni flow phenomenon.^[52] By mixing the high-boiling point solvent, dodecane, and the low-boiling point solvent, hexane, we obtain a controlled droplet ejection and evaporation during printing process. The expected adhesion and shape of the pattern could be estimated by contact angle measurement of droplets on the selected substrate. According to the Young's equation, the contact angle value provides the hydrophilic/hydrophobic relation between the surface tension of printed perovskite material and the surface energy of the surface substrate. **Figure 1a** demonstrates a contact angle around 25° of CsPbBr₃ NCs inkjet printed on SiO₂ for characterization. Once the jettability is achieved, we can control the printing on several substrates tuning the printer parameters obtaining high definition patterns (**Figure 1b–d**).

2.2. Morphology and Roughness of Inkjet Printed CsPbBr₃ NCs

We report the printing of high-quality CsPbBr₃ NCs layers on different substrates including flexible ones (**Figure 1c,d**). In addition to the optimization of the ink rheology and the printing procedure, the curing effect for solvent evaporation is crucial. To determine the best possible conditions for curing, we have investigated post-deposition annealing thermal treatments such as conventional hotplate, convection oven or inside a controlled thermal vacuum chamber. **Figure 2** shows a summary of the three different annealing processes employed to reach a final compact pinholes-free layer of CsPbBr₃ NCs.

A combination of atomic force microscopy (AFM) and field emission scanning electron microscopy (FESEM) inspections are performed to assess the surface morphology and roughness

of the inkjet-printed CsPbBr₃ layers after thermal treatment curing processes. AFM images are acquired on CsPbBr₃ NCs layers, deposited by inkjet on Si/SiO₂ substrates and then cured, as proposed in the Experimental Section, in order to facilitate the solvents evaporation and island growth. **Figure 3a–c** shows the AFM panel of images of different curing processes for a typical CsPbBr₃ inkjet-printed layer. The layers annealed in vacuum show the lowest roughness among the proposed thermal post-processes. Indeed, the sample exhibits a root mean square (rms) roughness value around $\approx 5\text{--}7$ nm, due to the aggregation of bigger NCs, with an average NC grain size around $10\text{--}12$ nm (**Figure 3a**). Therefore, the printed layers consist of compact and uniformly aggregated NCs of size lower than 12 nm as expected from the NCs present in the ink solution. The thermal annealing on convection oven and hotplates are less performing than vacuum annealing as can be observed in **Figure 3b,c**, where a roughness of the layers is about $15\text{--}25$ nm, and grain sizes around $\approx 50\text{--}100$ nm (**Figure 3d,f**). The difference of structures between the thermal treatments can be associated with different types of solvent evaporation and grain growth of the nanocrystalline layers when submitted to the annealing steps at different atmosphere and temperature (215°C). Hotplate and convection oven at atmospheric pressure induce non-uniform solvent evaporation and, according with **Figure 3**, the nanocrystals tend to aggregate and grow indicating insufficient surface encapsulation. On the contrary, vacuum annealing induces uniform and fast solvent evaporation maintaining the nanocrystals with ligands encapsulation and reducing their aggregation, in a similar way to the anti-solvent process in spin coating deposition methods.^[29,30] When annealed in vacuum, the lower grain size observed by microscopy is corresponded with a higher crystallinity (**Figure S3**, Supporting Information), possibly indicating better crystalline structure of the outer nanoparticle shell. Atoms lying in well-defined crystal structures require higher activation energies to evolve into new scenarios (such larger grains) and therefore a matrix of lower size grain is observed. Consequently, the grain growth process is delayed and that translates into a

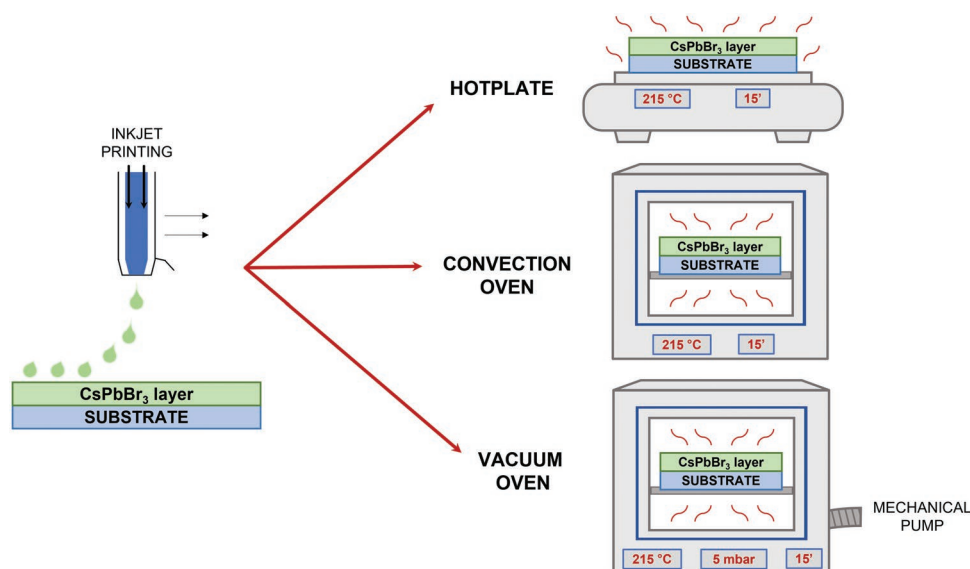


Figure 2. Workflow of proposed inkjet-printed CsPbBr₃ thin films obtained by several annealing as post-process.

smoother and denser surface of the printed layer for the vacuum annealing (Figure S3, Supporting Information) which has been shown as suitable for lightening applications.^{[31],[35]}

FESEM images reveal that the inkjet-printed CsPbBr₃ layers are homogeneous and they exhibit a large scale uniformity without a detrimental defects like pinholes or propagation of printing errors, such as large wrinkles or fractures among grains. However, a clear difference among the different curing processes can be detected, as observed by AFM technique: there are some local instabilities, see Figures 3d–f, which appear at the surface of the layers in the case of annealing process with hotplate or conventional oven (inhomogeneities with sizes around 100–200 nm that, in some particular places, reaches up to 500 nm in the case of hotplate).

Chemical modification of the ink might occur during the printing process, hence compromising the expected quality of the inkjet printed CsPbBr₃ NCs films. Further to this, during the annealing process, crystal growth and coalescence of grains^[53] can occur on the nanocrystalline layer.^[53] For this reason, X-ray diffraction (XRD), X-ray photoelectron spectroscopy (XPS), and Fourier transform infrared spectroscopy (FT-IR) are essential to investigate crystalline structure, elemental composition and chemical bonding.

2.3. Crystalline Structure by XRD

Figure 4a displays the X-ray diffraction pattern acquired from the printed CsPbBr₃ thin films on Si. The diffractogram clearly

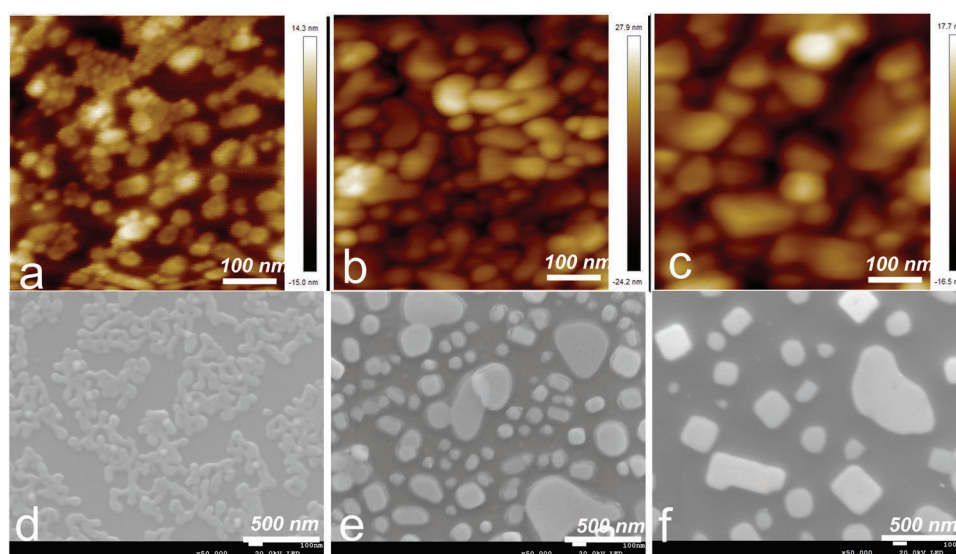


Figure 3. AFM top view topography of CsPbBr₃ NCs under different curing thermal treatment post-process: a) vacuum oven, b) convection oven, c) hotplate; SEM images of CsPbBr₃ under different curing thermal treatment post-process: d) top view printed layer after vacuum oven annealing; e) top view printed layer after hotplate annealing; f) top view printed layer after convection oven annealing.

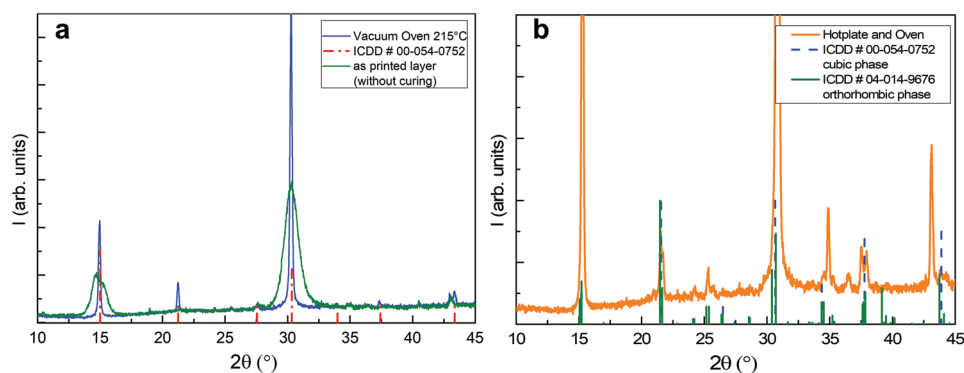


Figure 4. XRD pattern of inkjet-printed CsPbBr₃ a) after vacuum annealing and b) after hotplate and convection oven annealing at 215 °C.

exhibits the characteristic reflections of the cubic phase as expected from the nature of the NCs with peaks at $2\theta = 15.18^\circ$, 21.55° , 26.48° , 30.64° , 37.56° , and 43.62° , corresponding to the signature of cubic phase crystalline CsPbBr₃, with the JCPDS file number 00-054-0752 [Pm $\bar{3}$ m (221), $a = b = c = 5.83$ Å]. These signals are attributed to the {100}, {110}, {111}, {200}, {210}, and {211}, {220} reflecting planes, respectively.^[54,55] The cubic phase of perovskites CsPbBr₃ NCs is the most stable and well-studied structure according to the experimental and theoretical investigations in the previously reported studies at temperature above 117 °C.^[20,56] The intensity of the {100}, {110}, and {200} reflections evidence the structural order and preferential orientation of the inkjet-printed CsPbBr₃ NCs. The selection of the right temperature of curing was determined by an in-depth study of XRD versus thermal curing temperature. Increasing the temperature of the vacuum annealing process from ambient conditions, other phases (it should be noticed that the CsPb₂Br₅ phase appears with a characteristic peak at $2\theta = 11.7^\circ$ when the annealing temperature is below 200 °C)^[56,57] or recrystallization structures were observed until a clearly stable cubic phase is reached at 215 °C. This value is strictly correlated to the complete evaporation of selected high boiling point dodecane (215 °C) as ink vehicle. In particular, the specimens evidenced the absence of the characteristic double-peaks of tetragonal or orthorhombic CsPbBr₃ phases, which predict less stable and easily perishable printed layers.^[20,56]

In addition, hotplate and convection oven curing post-processes promote a standard orthorhombic phase as the crystal structure of CsPbBr₃, where the notable difference between the cubic and orthorhombic diffractogram is the splitting of reflections at 15.18° , 30.64° and the presence of new weak reflections at 24.16° , 25.1° , 28.58° which could be also observed clearly, (Figure 4b).^[58,59] In these last case, the orthorhombic structure is described with the Pnma space group (sometimes defined also as Pbnm due a different origin choice) and cell parameters are $a = 8.255$ Å, $b = 11.759$ Å, and $c = 8.207$ Å (JCPDS file number 04-014-9676).^[60,61]

2.4. Evaluation of the Amount of Solvent in Printed Layers by FTIR

If the annealing process is not able to evaporate all the solvents, then alkane binary mixtures (low/high boiling point hexane/dodecane) could remain in the layers. This is known

to decrease the crystallinity, affect negatively optical and electrical properties, and cause further degradation. To quantify the solvents still present in the nanocrystalline CsPbBr₃ layers is crucial to understand bonding structure and compositional variations. The most direct way to detect solvent features is by looking to the infrared spectra, which was measured by FT-IR. The acquired spectra are displayed in **Figure 5**, in the range from 400 to 3200 cm⁻¹, which shows the absorbance of CsPbBr₃ ink (blue line), annealed inkjet-printed CsPbBr₃ layer (black line), and ink solvents (red line). The peaks correspond to reported functional vibrations of dodecane and hexane, -CH and =CH stretching at around 2860 and 3000 cm⁻¹, respectively, C-H methyl rock at 1378 cm⁻¹ and C-H scissoring at 1465 cm⁻¹.^[62] While the presence of these peaks is clear in the ink and in the solvents, they are absent in the printed layer, indicating that the vacuum thermal curing process has been able to evaporate all the solvents. The ligands of oleic acid (OA) and oleylamine (OAm), employed in the hot injection process, are not detected by the FTIR spectrum as expected at the absorption features at 1535 and 1710 cm⁻¹, ascribed to the oleate anions (-COO-) and C=O stretching vibrations. Possibly because their content is very low, and they are enveloped within the NP layer.^[62-64] The observed peaks (black line) in the range from 400 to 1200 cm⁻¹ are related to the substrate signal due to the negligible intensity of above mentioned contributions after annealing process.

2.5. Composition and Local Bonding by XPS

To obtain deeper insights in the chemical environment and composition of perovskite inkjet-printed films, XPS analysis was conducted. Here, it was mainly identified the presence of Cs, Pb, and Br in each sample. Then, it was necessary to obtain high-resolution (HR) XPS spectra of these elements. HR-XPS spectra of the inkjet-printed CsPbBr₃ thin films exhibit the corresponding Cs 3d, Pb 4f, and Br 3d doublets, which were centered at binding energies (BEs) $\approx 724.0/738$, $138.0/143.7$, and $68.9/69.9$ eV, respectively, in line with the characteristics of CsPbBr₃ in literature data.^[65-67] Charge and BEs for all the species are corrected to adventitious carbon at 284.8 eV.

To investigate the effect of diverse annealing processes such as hotplate (HPL), convection oven (CO) and vacuum oven (VO) on the surface properties of inkjet-printed perovskite

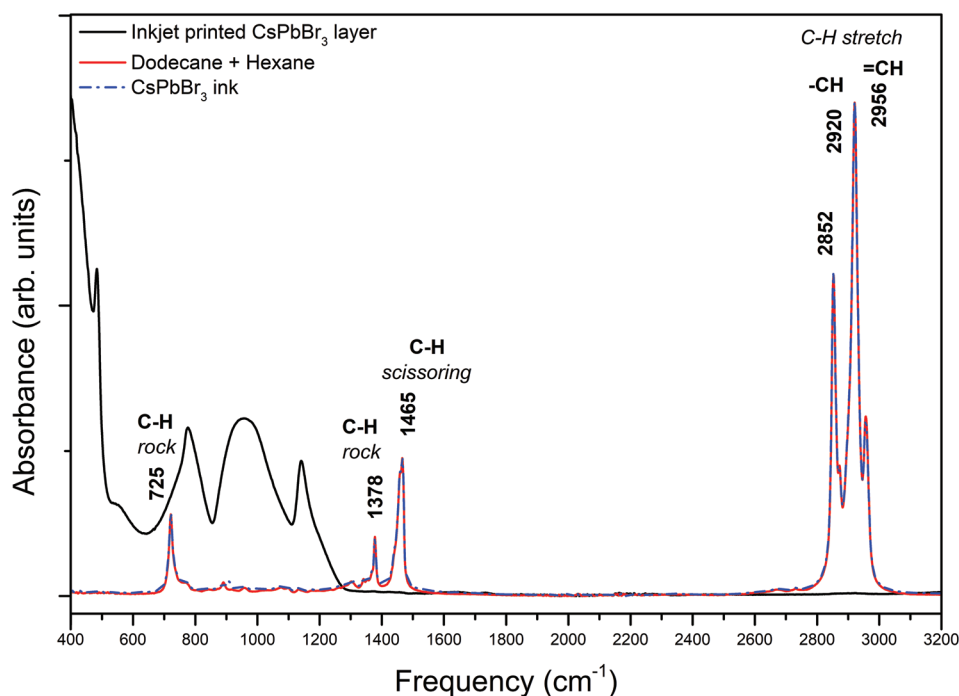


Figure 5. FT-IR spectra comparison between the CsPbBr₃ ink and inkjet-printed layer after annealing in vacuum oven at 215 °C.

quantum dots (PeQDs) layers, first, HR-XPS Pb 4f spectra were fitted and analyzed. As can be observed in **Figure 6a**, the Pb doublets were decomposed in two additional Pb 4f_{7/2} and Pb 4f_{5/2} signals: the first one located at 138.0/142.9 eV ascribed to Pb²⁺ coming from CsPbX₃ structure, while the second one at 138.6/143.6 eV for HPI and 138.9/143.7 eV for CO, associated to the presence of PbBr₂. These species were only observed for the films that undergo HPI and CO,^[65,66] indicating that annealing treatments favor the PbBr₂ diffusion to the material surface. The emergence of PbBr₂ allows to suggest that HPI and CO can facilitate the eventual degradation of the PeQDs, which is not observable for VO. This strategy ensures the formation of 3D perovskite cubic phase, without the appearance of secondary species. Lastly, in the samples under study there is no contribution of metallic Pb⁰ expected at 136.5 eV,^[68] which is an indication that PeQDs films treated with the different annealing processes show a low density of undercoordinated Pb, at least not identified in this contribution.

Figure 6b shows the HR-XPS Br 3d spectra of the post-treated inkjet-printed PeQDs layers, clearly showing the well-defined Br 3d_{5/2} and Br 3d_{3/2} signals, attained to the formation of Cs–Br/Pb–Br bonds in the perovskite structure.^[66] Then, by detailing the fitting of the Br 3d spectra for all the annealed samples, we observe that the one from VO depict the highest intensity, compared with HPI and CO. This difference is attributed to the more stoichiometric CsPbBr₃ PeQDs surface composed by Cs–Br and Pb–Br interactions under VO than that of HPI and CO treatments. Simultaneously, it is also possible to evidence the formation of Cs–Br bonds in the HR-XPS Cs 3d spectra through the Cs 3d_{5/2} and Cs 3d_{3/2} peaks (see Figure 6c). As carried out with Br signals, the fitting of the Cs 3d spectra obtained for the films under VO curing is, as expected, close to the ideal values of literature,^[67] meanwhile, the Cs 3d signals coming from the films treated with HPI and CO are less intense and present a Cs⁺ deficiency. To corroborate this affirmation, we have estimated the chemical composition of

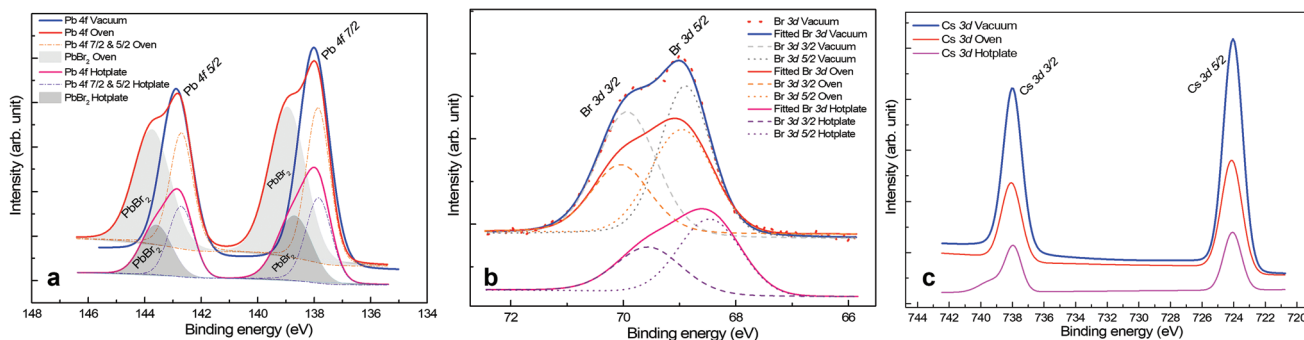


Figure 6. High-resolution XPS spectra corresponding to a) Pb 4f, b) Cs 3d, and c) Br 3d in annealed CsPbBr₃ thin film at 215 °C for 15 min, deposited on Si substrate. The curves represent the experimental data with the fit of the corresponding peaks.

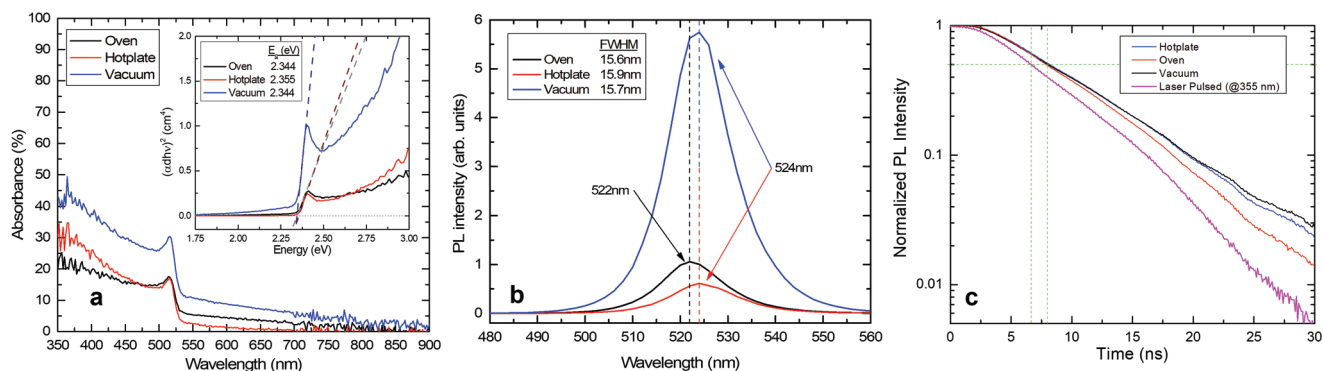


Figure 7. a) UV-vis characterization of inkjet-printed CsPbBr₃ with expected signals for this LHP; b) PL spectra of the three different thermal post-processes selected; c) time resolved PL of the three different CsPbBr₃ printed thin films.

the PeQDs films post-treated with HPL, CO and VO. Through employing tabulated sensitivity factors from the area intensities (Table S2, Supporting Information), an effective stoichiometry ratio (Cs:Pb:Br) of 1:1:3 resulted for the inkjet-printed PeQDs layers annealed VO. Taking into account HR-XPS Pb 4f and Br 3d spectra, we estimate that the atomic ratio of Br/Pb is derived to be ≈ 3 , indicating a good stoichiometry in the surface region of the after VO curing. An adequate stoichiometry allows to achieve a less defective material with good PL properties. On the other hand, the samples annealed under HPL and CO present a non-stoichiometric ratio (Cs:Pb:Br) $\approx 0.5:1.5:3$, which is detrimental for the PL emission. Accordingly, we can conclude that inkjet-printed layers treated with VO shows a stoichiometric PeQDs surface where Pb²⁺ species is bonded to Br and forming the [PbBr₆] octahedra from the perovskite structure. This feature disagrees for the inkjet-printed PeQDs films treated under HPL and CO, where Cs⁺ defects are detected in the material surface, being detrimental for the photoluminescence (PL) properties, as we explain below.

2.6. Optical Properties of Inkjet Printed CsPbBr₃ Layers

The optical absorption and emission properties are crucial for the application of CsPbBr₃ layers in optoelectronics (LEDs). All the inkjet-printed layers have been measured to obtain absorption, reflection, and PL. These measurements have allowed to determine refractive index, absorption coefficient and bandgap energy. In addition, from PL measurements we have determined exciton features, Stokes shift, PLQY and decay times. All this information is essential to assess the quality of the printed layers and validate the printing procedure and the vacuum annealing as the optimum choices for high performance layers for color conversion and LEDs. For the PL measurements we have used an excitation wavelength of 325 nm in the UV (3.82 eV) which is well above the band-gap expected for CsPbBr₃. **Figure 7a,b** respectively show the absorption and PL spectra of the three different selected thermal post-processes. All the spectra exhibit similar absorption transitions. First of all, they present an absorption edge around 524 nm. It can also be observed that the exciton feature of the sample undergo to vacuum annealing is more intense and well defined. This has to do with a better crystallinity of this sample and the less

presence of disordered tail states. The values of the bandgap have been determined from the Tauc plots after subtracting the excitonic emission and yields ≈ 2.35 eV for the three samples. Moreover, the three samples present very similar PL wavelength (524 nm) with a narrow quasi-Lorentzian shape and full width at half-maximum (FWHM) of only 16 nm (72 meV), which is very close to the best values reported in the literature.^[69] The remarkable reduced intensity of the HPL and CO annealed films is due to the increased presence of aggregates of NCs observed by SEM and AFM, which quench the emission of the underlying nanocrystalline layer.

A very narrow spectral width is usually attributed to a high quality monodisperse size distribution of NCs, which also shows distinct excitonic peaks in the absorption. The emission of the PeQDs in the colloidal solution is at 514 nm (2.41 eV) with a FWHM of 15 nm and this fact suggests that size distribution in solution and in the printed layers is quite similar, with only slightly larger NCs in the printed layers. In fact, this is in agreement with the larger NCs observed in the AFM and SEM images (see above). Nevertheless, we have to remark that the sample annealed in VO exhibits the highest PLQY $\approx 20\%$. On the other hand, with the hotplate and convection oven, the maximum PLQY reached is around 5%. These values are lower than the pristine ink solution, PLQY of 87%, indicating that the CsPbBr₃ nanoparticles were aggregating at the expense of the surface ligands.^[53] Under annealing treatment, it is well known that some fraction of capping ligands covering the PeQDs surface are detached, promoting the perovskite agglomeration with the aim to decrease their surface energy.^[70] In this way, intra-bandgap energy levels emerge into the big particles, favoring the non-radiative recombination mechanism, and blocking the radiative channel.^[71] In the case of films treated with HPL and CO, the presence of Cs⁺ defects observed through XPS analysis could be reason to quench their characteristic PL features. However, as we discussed above, annealing treatment supports the preparation of PeQDs films with low density of pinholes/printing errors. Therefore, PeQDs films treated with VO are good candidates to fabricate efficient optoelectronic devices.

These results demonstrate that the vacuum annealed sample brings about the highest crystallinity and purity of the optical features while it shows by far the highest PLQY and thus is expected to be the optimum processing in terms of optical performance. **Figure 7c** shows the PL response of the CsPbBr₃ samples

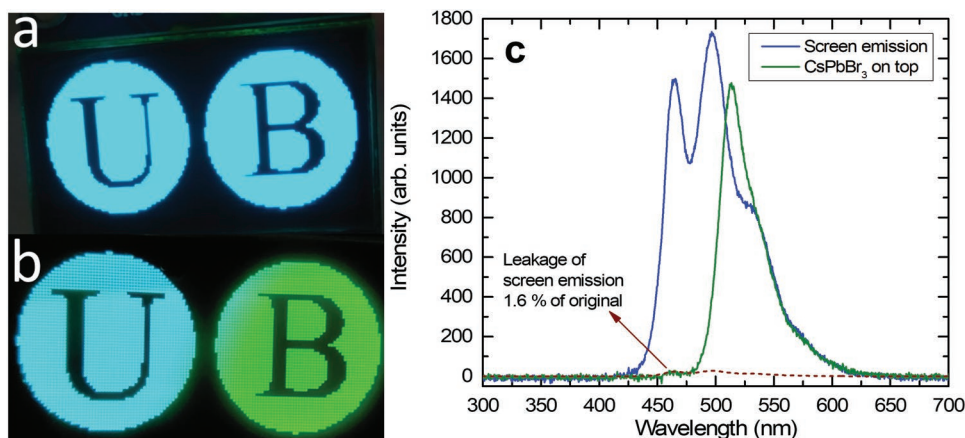


Figure 8. Optical photo of the CsPbBr₃ perovskite CCL excited by the back blue InGaN-based micro-LED display a) before and b) after printing the CsPbBr₃. c) Emission spectra of the screen emission and the printed layer.

submitted to different annealing, together with the recorded pulse directly reflected from the laser. It is clear from the figure that the emission coming from the samples is slightly slower than the one coming from the laser, indicating that the emission response lays within the nanosecond range. Analyzing the time evolution of the observed emission of the samples, by deconvoluting the laser response (which also incorporate the response of our detection system), we found a that the emission follows an exponential, with decay times around 2.0, 2.5, and 2.7 ns for the samples annealed in hotplate, oven, and vacuum, respectively. The fast emitting process means an excellent luminescent performance due to the feature of exciton recombination in the CsPbBr₃ film.

2.7. Preparation of Color Converted Layers

The inkjet-printed CsPbBr₃ thin films, with high PLQY, when annealed in vacuum oven at low temperatures, pave the way for their use in lighting and display over illuminated substrates.^[72] A prove of this flexibility is their application in the form of back-lighting, which combines blue InGaN chips with the inkjet-printed CsPbBr₃ thin films as CCL. **Figure 8** demonstrates the feasibility of CCL onto benchmarking display (blue emitting display UB letters), where the inkjet-printed CsPbBr₃ thin film onto the pixels of only the letter B ensures a controlled wavelength emission (color selectivity) reaching high color rendering index (combining red emission, Figure S5, Supporting Information) and widening the color gamut shape. The spectra in Figure 8c of both the screen and the printed layer confirm that the leakage of blue emission is minimum when the CsPbBr₃ layer is printed on top, i.e., 1.6% of the original. These characteristics are promising milestones to improve the definition of current display protocol based on white LED, TFT, and liquid crystal.

3. Conclusions

In this work, we demonstrated the formulation and printability of CsPbBr₃ NCs ink by using inkjet printing technology to

obtain highly emissive green thin films with outstanding optical performance, large area, high reliability, and low-cost manufacturing. We successfully inkjet-printed CsPbBr₃ perovskite thin films demonstrating uniform surface and low roughness. The well-known coffee ring issue was solved by selecting the ratio of a high-boiling point solvent dodecane with a low-boiling point solvent hexane. We proved the importance of selecting the post-process annealing comparing three common solutions: hotplate, convection oven and vacuum oven. We verified that vacuum oven it is the most appropriated annealing process by morphological, chemical and optical characterization. Excellent photoluminescence with narrow FWHM value of 16 nm (72 meV), PLQY up to ≈20% after annealing process under VO, and high stability are achieved. Excited samples at room temperature are generating exciton recombination with binding energies of 40 meV. Taking advantage of the controlled and homogeneous printed layer and its outstanding morphological and optical properties, a pure green CCL is easily fabricated.

4. Experimental Section

Synthesis of CsPbBr₃ Colloidal Solutions: The CsPbBr₃ nanoparticles (NPs) have been synthesized by following the hot-injection method described by Kovalenko and co-workers (Protesescu L. et al., J. Navarro-Arenas et al.),^[69,73] adding some modifications.^[74] All the reactants were used as received without additional purification process. First, to prepare a Cs-oleate solution, 0.41 g of Cs₂CO₃ (Sigma-Aldrich, 99.9%), 1.5 mL of oleic acid (OA, Sigma-Aldrich, 90%) and 20 mL of 1-octadecene (1-ODE, Sigma-Aldrich, 90%) were loaded together into a 50 mL three-neck flask and degassed at 120 °C in vacuum for 1 h with constant stirring. Then, the mixture was N₂-purged and heated to 150 °C, completely dissolving the Cs₂CO₃. The solution was stored under N₂, keeping the temperature at 120 °C to prevent Cs-oleate oxidation.

Secondly, 0.85 g of PbBr₂ (ABCRC, 99.999%) were mixed with 50 mL of 1-ODE into a 100 mL three-neck flask. The mixture was heated at 120 °C in vacuum for 1 h with constant stirring. Then, 10 mL of a preheated mixture of OA and oleylamine (5 mL each one, 130 °C) (OLA, Sigma-Aldrich, 98%) were added to the flask under N₂, and the mixture was quickly heated to 170 °C. Simultaneously, 4 mL of Cs-oleate solution was swiftly added to the mixture and then, immersed into an ice bath for 5 s to quench the reaction. To perform the isolation process of the NPs, 60 mL of methyl acetate (99.5%, Sigma-Aldrich) was added to 30 mL

of liquor solution, and the colloidal solutions were centrifugated at 5000 rpm for 10 min. Then, NP pellets were separated after discarding the supernatant and redispersed in dodecane to concentrate the NPs at 50 mg mL⁻¹.

Preparation of Inks Based on CsPbBr₃ Nanocrystals: The colloidal solution of CsPbBr₃ NCs in dodecane was further dissolved in hexane (3:1) with the obtained colloidal solutions being stirred and sonicated until collecting the supernatant. The filtered solution of perovskite nanocrystal ink was printed with a fixed drop-volume of 10 pL through 21- μ m diameter nozzle by using an adequate cartridge for Dimatix printers (Fujifilm Dimatix Inc.) on selected previously cleaned substrates. 10–20% of solid content weigh concentration with a viscosity around \approx 3 cP were used. The preparation of the inks was carried out in a glove box while the printing proceeded under ambient conditions (inert box).

Four different substrates were employed for printing the layers: silicon (Si), silica on silicon (SoS), fused silica (FS), and flexible polyimide (PI). The substrates were cleaned by an ultrasonicator with detergent (Hellmax, 1 mL over 100 mL deionized water), acetone, deionized water, and isopropanol for 20 min each and then treated with UV light for 10 min. The ink stability was assessed by Turbiscan LabExpert, connected to a cooling TLab Cooler system. The steady shear viscosity measurements were performed using a rotational Discovery Series Hybrid Rheometer (DHR-1) instrument equipped with integrated magnetic cylinder geometry. Particle size measurements were performed by light scattering. Photon Correlation Spectrometer (3DDLS LS Instruments) that performs dynamic and static light scattering (DLS and SLS, respectively) measures between 20° and 140°. This instrument, equipped with a He–Ne (632.8 nm) laser, incorporates a 3D cross-correlation technology which eliminates the contribution of multiple light scattering and permits to measure turbid samples. The software automatically estimates particle size distribution using Cumulant fit and CONTIN analysis. The contact angle was determined using an instrument (JC200C1, Powereach, China) at room temperature.

Inkjet Printing and Thermal Treatments of CsPbBr₃ NCs Layers: The details of the printing procedure for the CsPbBr₃ NCs inks were planned based on mixing high/low boiling point solvents,^[26,38,75] dodecane and hexane (3:1). An ink ejection frequency of 2.0 kHz and a resolution of 500–450 drops in.⁻¹ (DPI) was used, further details of inkjet set up can be found in Table S1 (Supporting Information). During the CsPbBr₃ NC layer printing, the substrate temperature was kept constant at 50 °C in order to attain a proper adhesion among the different sublayers piled up to complete the thick full layer. After the inkjet-printing process, the layers were submitted to the curing process using three different annealing methods: hotplate, convection oven and vacuum oven.

Layer Morphology, Structure, Composition, and Optical Properties: The morphology and structure of Inkjet-printed perovskite thin films were studied by FESEM using a FEI Nova 200 instrument (JEOL J-7100 microscope). The surface roughness was evaluated using an AFM Digital Instruments Nanoscope D-5000, by scanning the x–y plane, with a z-axis resolution limit of around 1 nm. The crystalline microstructure, orientation and size of the NCs were determined by XRD using a Japan Rigaku D/Max-IIA X-ray diffractometer using Cu K α radiation, $\lambda = 1.5406$ Å, operating at 40 keV and 40 mA. The analysis of the chemical composition and environment of the perovskite NCs printed layers was performed using a PHI ESCA-5500 X-ray photoelectron spectrometer with a monochromatic Al K α radiation ($E = 1486$ eV) at 350.0 W with the X-ray source and detector forming an angle of 45.1° with the normal of the sample. The thickness of the printed layers was estimated using the profilometer DEKTAK 6M (Veeco Instruments).

The presence of the different remaining compounds adsorbed on the lead-free perovskite surfaces was analyzed by a Thermo Scientific Systems NICOLET iN10 FT-IR spectrometer equipped with a DTGS detector, in the far-IR in the range from 4000 to 220 cm⁻¹. The optical properties were evaluated by measuring the transmittance and reflectance spectra, by using an integrating sphere (Bentham PV300 EQE system), using monochromated light from a Xe and quartz halogen dual lamp source through the 300–1100 nm range, and collecting the transmitted (or reflected) light with an InGaAs photodetector. Finally, the

emission properties were determined by acquiring photoluminescence (PL) spectra of the films grown onto Si substrates, exciting the samples with the 325-nm line of a He–Cd laser, with a power density of 8×10^3 W cm⁻², and analyzing the emitted light with a single-grating monochromator coupled to a GaAs photomultiplier. Time-resolved PL (TRPL) measurements were performed using the 355-nm line from the third harmonic of a Nd:YAG laser, working with pulses with a duration of 5 ns. The emission was sent to a monochromator and the time response was acquired at the maximum wavelength of emission, 520 nm. The emission was recorded using a GaAs photomultiplier tube and the resulting current signal was analyzed by a digital oscilloscope.

Supporting Information

Supporting Information is available from the Wiley Online Library or from the author.

Acknowledgements

The authors wish to thank the financial support from the European Commission via FET Open Grant (862656 – DROP-IT), MINECO (Spain) for grant PID2019-105658RB-I00 (PRITES project), Ministry of Science and Innovation of Spain under Project STABLE (PID2019-107314RB-I00), and Generalitat Valenciana via Prometeo Grant Q-Devices (Prometeo/2018/098). J.L.F. acknowledges the financial support from the Spanish Ministry of Education, Culture and Sports (FPU16/06257).

Conflict of Interest

The authors declare no conflict of interest.

Data Availability Statement

The data that support the findings of this study are available from the corresponding author upon reasonable request.

Keywords

perovskites, quantum dots, green emission, inkjet printing, nanocrystals, color conversion layers, CsPbBr₃

Received: November 18, 2021

Revised: December 23, 2021

Published online:

- [1] A. M. Bagher, *Int. J. Adv. Res. Phys. Sci. (IJARPS)* **2017**, *4*, 2349.
- [2] N. K. Kumawat, X.-K. Liu, D. Kabra, F. Gao, *Nanoscale* **2019**, *11*, 2109.
- [3] C. Liang, P. Li, H. Gu, Y. Zhang, F. Li, Y. Song, G. Shao, N. Mathews, G. Xing, *Sol. RRL* **2018**, *2*, 1700217.
- [4] B. Geffroy, P. le Roy, C. Prat, *Polym. Int.* **2006**, *55*, 572.
- [5] N. Sain, D. Sharma, P. Choudhary, *Int. J. Eng. Appl. Sci. Technol.* **2020**, *4*, 587.
- [6] J. L. Friero, C. Guillaume, J. López-Vidrier, O. Blázquez, S. González-Torres, C. Labbé, S. Hernández, X. Portier, B. Garrido, *Nanotechnology* **2020**, *31*, 465207.
- [7] J. L. Friero, O. Blázquez, J. López-Vidrier, L. López-Conesa, S. Estradé, F. Peiró, J. Ibáñez, S. Hernández, B. Garrido, *Phys. Status Solidi A* **2017**, *1700451*, 1700451.

- [8] F. Mathies, E. J. W. List-Kratochvil, E. L. Unger, *Energy Technol.* **2020**, 8, 1900991.
- [9] S. Lou, T. Xuan, J. Wang, *Opt. Mater.: X* **2019**, 1, 100023.
- [10] S. Adjokatse, H.-H. Fang, M. A. Loi, *Mater. Today* **2017**, 20, 413.
- [11] M. Yang, Z. Li, M. O. Reese, O. G. Reid, D. H. Kim, S. Siol, T. R. Klein, Y. Yan, J. J. Berry, M. F. A. M. van Hest, K. Zhu, *Nat. Energy* **2017**, 2, 17038.
- [12] M. I. H. Ansari, A. Qurashi, M. K. Nazeeruddin, *J. Photochem. Photobiol., C* **2018**, 35, 1.
- [13] A. F. Gualdrón-Reyes, S. Masi, I. Mora-Seró, *Trends Chem.* **2021**, 3, 499.
- [14] D. Luo, Q. Chen, Y. Qiu, M. Zhang, B. Liu, *Nanomaterials* **2019**, 9, 1007.
- [15] J. Mao, H. Lin, F. Ye, M. Qin, J. M. Burkhardtmeier, H. Zhang, X. Lu, K. S. Wong, W. C. H. Choy, *ACS Nano* **2018**, 12, 10486.
- [16] Y. Jiang, C. Qin, M. Cui, T. He, K. Liu, Y. Huang, M. Luo, L. Zhang, H. Xu, S. Li, J. Wei, Z. Liu, H. Wang, G.-H. Kim, M. Yuan, J. Chen, *Nat. Commun.* **2019**, 10, 1868.
- [17] S. Chen, C. Chen, C. Bao, M. Mujahid, Y. Li, P. Chen, Y. Duan, *Molecules* **2019**, 24, 800.
- [18] Z.-K. Tan, R. S. Moghaddam, M. L. Lai, P. Docampo, R. Higler, F. Deschler, M. Price, A. Sadhanala, L. M. Pazos, D. Credgington, F. Hanusch, T. Bein, H. J. Snaith, R. H. Friend, *Nat. Nanotechnol.* **2014**, 9, 687.
- [19] W. Qiu, Z. Xiao, K. Roh, N. K. Noel, A. Shapiro, P. Heremans, B. P. Rand, *Adv. Mater.* **2019**, 31, 1806105.
- [20] L. Protesescu, S. Yakunin, M. I. Bodnarchuk, F. Krieg, R. Caputo, C. H. Hendon, R. X. Yang, A. Walsh, M. V. Kovalenko, *Nano Lett.* **2015**, 15, 3692.
- [21] H. Yu, G. Tian, W. Xu, S. Wang, H. Zhang, J. Niu, X. Chen, *Front. Chem.* **2018**, 6, 381.
- [22] S. Yuan, Z. K. Wang, M. P. Zhuo, Q. S. Tian, Y. Jin, L. S. Liao, *ACS Nano* **2018**, 12, 9541.
- [23] Y. Li, Y. Lv, Z. Guo, L. Dong, J. Zheng, C. Chai, N. Chen, Y. Lu, C. Chen, *ACS Appl. Mater. Interfaces* **2018**, 10, 15888.
- [24] C. H. Tien, L. C. Chen, K. Y. Lee, Z. L. Tseng, Y. S. Dong, Z. J. Lin, *Energies* **2019**, 12, 3507.
- [25] M. Singh, H. M. Haverinen, P. Dhagat, G. E. Jabbour, *Adv. Mater. (Deerfield Beach, Fla.)* **2010**, 22, 673.
- [26] A. Kamysshny, S. Magdassi, *Inkjet-Based Micromanufacturing*, Wiley-VCH Verlag GmbH & Co. KGaA, Weinheim, Germany **2012**.
- [27] G. Vescio, G. Martin, A. Crespo, S. Claramunt, D. Alonso Rodrigo, J. Lopez-Vidrier, S. Estradé, M. Porti, R. Rodríguez, F. Peiró, A. Cornet, A. Cirera, M. Nafria, *ACS Appl. Mater. Interfaces* **2019**, 11, 23659.
- [28] G. Vescio, J. López-Vidrier, R. Leghrib, A. Cornet, A. Cirera, *J. Mater. Chem. C* **2016**, 4, 1804.
- [29] Z. Li, P. Li, G. Chen, Y. Cheng, X. Pi, X. Yu, D. Yang, L. Han, Y. Zhang, Y. Song, *ACS Appl. Mater. Interfaces* **2020**, 12, 40987.
- [30] C. Liang, P. Li, H. Gu, Y. Zhang, F. Li, Y. Song, G. Shao, N. Mathews, G. Xing, *Sol. RRL* **2018**, 2, 1700217.
- [31] F. Hermerschmidt, F. Mathies, V. R. F. Schröder, C. Rehermann, N. Z. Morales, E. L. Unger, E. J. W. List-Kratochvil, *Mater. Horiz.* **2020**, 7, 1773.
- [32] L. Shi, L. Meng, F. Jiang, Y. Ge, F. Li, X. gang Wu, H. Zhong, *Adv. Funct. Mater.* **2019**, 29, 1903648.
- [33] D. Li, J. Wang, M. Li, G. Xie, B. Guo, L. Mu, H. Li, J. Wang, H. L. Yip, J. Peng, *Adv. Mater. Technol.* **2020**, 5, 2000099.
- [34] D. Bi, C. Yi, J. Luo, J. D. Décoppet, F. Zhang, S. M. Zakeeruddin, X. Li, A. Hagfeldt, M. Grätzel, *Nat. Energy* **2016**, 1, 16142.
- [35] I. A. Howard, T. Abzieher, I. M. Hossain, H. Eggers, F. Schackmar, S. Ternes, B. S. Richards, U. Lemmer, U. W. Paetzold, *Adv. Mater.* **2019**, 31, 1806702.
- [36] A. Gao, J. Yan, Z. Wang, P. Liu, D. Wu, X. Tang, F. Fang, S. Ding, X. Li, J. Sun, M. Cao, L. Wang, L. Li, K. Wang, X. W. Sun, *Nanoscale* **2020**, 12, 2569.
- [37] C. C. Ilie, F. Guzman, B. L. Swanson, I. R. Evans, P. S. Costa, J. D. Teeter, M. Shekhirev, N. Benker, S. Sikich, A. Enders, P. A. Dowben, A. Sinitkii, A. J. Yost, *J. Phys. Condens. Matter* **2018**, 30, 18LT02.
- [38] M. Duan, Z. Feng, Y. Wu, Y. Yin, Z. Hu, W. Peng, D. Li, S. jih Chen, C. Y. Lee, A. Lien, *Adv. Mater. Technol.* **2019**, 4, 1900779.
- [39] F. Zhang, Z. Shi, S. Li, Z. Ma, Y. Li, L. Wang, D. Wu, Y. Tian, G. Du, X. Li, C. Shan, *ACS Appl. Mater. Interfaces* **2019**, 11, 28013.
- [40] C. Zheng, X. Zheng, C. Feng, S. Ju, Z. Xu, Y. Ye, T. Guo, F. Li, *Org. Electron.* **2021**, 93, 106168.
- [41] Y. Liu, F. Li, L. Qiu, K. Yang, Q. Li, X. Zheng, H. Hu, T. Guo, C. Wu, T. W. Kim, *ACS Nano* **2019**, 13, 2042.
- [42] S. Choi, S. Y. Lee, D. Y. Kim, H. K. Park, M. J. Ko, K. H. Cho, J. Choi, *J. Ind. Eng. Chem.* **2020**, 85, 226.
- [43] T. Xuan, S. Shi, L. Wang, H. C. Kuo, R. J. Xie, *J. Phys. Chem. Lett.* **2020**, 11, 5184.
- [44] Y. Yin, Z. Hu, M. U. Ali, M. Duan, L. Gao, M. Liu, W. Peng, J. Geng, S. Pan, Y. Wu, J. Hou, J. Fan, D. Li, X. Zhang, H. Meng, *Adv. Mater. Technol.* **2020**, 5, 2000251.
- [45] Y. Yin, M. U. Ali, M. Liu, J. Miao, W. Peng, D. Li, S. Chen, C. Lee, H. Meng, *Small* **2019**, 15, 1901954.
- [46] T. H. J. Van Osch, J. Perelaer, A. W. M. De Laat, U. S. Schubert, *Adv. Mater.* **2008**, 20, 343.
- [47] A. Kamysshny, S. Magdassi, *Small* **2014**, 10, 3515.
- [48] Shlomo Magdassi, S. Magdassi, *Pigm. Resin Technol.* **1987**, 16, 4.
- [49] D. Jang, D. Kim, J. Moon, *Langmuir* **2009**, 25, 2629.
- [50] D. Soltman, V. Subramanian, *Langmuir* **2008**, 24, 2224.
- [51] H. Hu, R. G. Larson, *J. Phys. Chem. B* **2006**, 110, 7090.
- [52] C. Seo, D. Jang, J. Chae, S. Shin, *Sci. Rep.* **2017**, 7, 500.
- [53] A. F. Gualdrón-Reyes, S. J. Yoon, E. M. Barea, S. Agouram, V. Muñoz-Sanjósé, Á. M. Meléndez, M. E. Niño-Gómez, I. Mora-Seró, *ACS Energy Lett.* **2019**, 4, 54.
- [54] M. Zhang, Z. Zheng, Q. Fu, Z. Chen, J. He, S. Zhang, L. Yan, Y. Hu, W. Luo, *CrystEngComm* **2017**, 19, 6797.
- [55] C. Tenaillon, S. Aharon, B. El Cohen, L. Etgar, *Nanoscale Adv.* **2019**, 1, 147.
- [56] G. Lozano, *J. Phys. Chem. Lett.* **2018**, 9, 3987.
- [57] X. Su, J. Zhang, G. Bai, *Bull. Mater. Sci.* **2018**, 41, 5.
- [58] M. S. Kirschner, B. T. Diroll, P. Guo, S. M. Harvey, W. Helweh, N. C. Flanders, A. Brumberg, N. E. Watkins, A. A. Leonard, A. M. Evans, M. R. Wasielewski, W. R. Dichtel, X. Zhang, L. X. Chen, R. D. Schaller, *Nat. Commun.* **2019**, 10, 504.
- [59] D. Malyshekin, V. Sereda, I. Ivanov, M. Mazurin, A. Sednev-Lugovets, D. Tsvetkov, A. Zuev, *Mater. Lett.* **2020**, 278, 128458.
- [60] M. Rodová, J. Brožek, K. Knížek, K. Nitsch, *J. Therm. Anal. Calorim.* **2003**, 71, 667.
- [61] F. Bertolotti, L. Protesescu, M. V. Kovalenko, S. Yakunin, A. Cervellino, S. J. L. Billinge, M. W. Terban, J. S. Pedersen, N. Masciocchi, A. Guagliardi, *ACS Nano* **2017**, 11, 3819.
- [62] G. Li, F. W. R. Rivarola, N. J. L. K. Davis, S. Bai, T. C. Jellicoe, F. De La Peña, S. Hou, C. Ducati, F. Gao, R. H. Friend, N. C. Greenham, Z. K. Tan, *Adv. Mater.* **2016**, 28, 3528.
- [63] J. Liu, K. Song, Y. Shin, X. Liu, J. Chen, K. X. Yao, J. Pan, C. Yang, J. Yin, L. J. Xu, H. Yang, A. M. El-Zohry, B. Xin, S. Mitra, M. N. Hedhili, I. S. Roqan, O. F. Mohammed, Y. Han, O. M. Bakr, *Chem. Mater.* **2019**, 31, 6642.
- [64] Q. Xie, D. Wu, X. Wang, Y. Li, F. Fang, Z. Wang, Y. Ma, M. Su, S. Peng, H. Liu, K. Wang, X. W. Sun, *J. Mater. Chem. C* **2019**, 7, 11251.
- [65] L. R. Pederson, *J. Electron Spectrosc. Relat. Phenom.* **1982**, 28, 203.
- [66] V. I. Nefedov, *J. Electron Spectrosc. Relat. Phenom.* **1977**, 12, 459.
- [67] Y. Wang, Y. Ren, S. Zhang, J. Wu, J. Song, X. Li, J. Xu, C. H. Sow, H. Zeng, H. Sun, *Commun. Phys.* **2018**, 1, 96.
- [68] A. Jaffe, Y. Lin, C. M. Beavers, J. Voss, W. L. Mao, H. I. Karunadasa, *ACS Cent. Sci.* **2016**, 2, 201.

- [69] L. Protesescu, S. Yakunin, M. I. Bodnarchuk, F. Krieg, R. Caputo, C. H. Hendon, R. X. Yang, A. Walsh, M. V. Kovalenko, *Nano Lett.* **2015**, *15*, 3692.
- [70] A. F. Gualdrón-Reyes, S. J. Yoon, E. M. Barea, S. Agouram, V. Muñoz-Sanjosed, Á. M. Meléndez, M. E. Niño-Gómez, I. Mora-Seró, *ACS Energy Lett.* **2019**, *4*, 54.
- [71] M. Vallés-Pelarda, A. F. Gualdrón-Reyes, C. Felip-León, C. A. Angulo-Pachón, S. Agouram, V. Muñoz-Sanjosed, J. F. Miravet, F. Galindo, I. Mora-Seró, *Adv. Opt. Mater.* **2021**, *9*, 2001786.
- [72] J. Arrese, G. Vescio, E. Xuriguera, B. Medina-Rodriguez, A. Cornet, A. Cirera, *J. Appl. Phys.* **2017**, *121*, 104904.
- [73] J. Navarro-Arenas, I. Suárez, V. S. Chirvony, A. F. Gualdrón-Reyes, I. Mora-Seró, J. Martínez-Pastor, *J. Phys. Chem. Lett.* **2019**, *10*, 6389.
- [74] E. Hassanabadi, M. Latifi, A. F. Gualdrón-Reyes, S. Masi, S. J. Yoon, M. Poyatos, B. Julián-López, I. Mora-Seró, *Nanoscale* **2020**, *12*, 14194.
- [75] V. Subramanian, T. Lee, *Nanotechnology* **2012**, *23*, 340201.